

Coincident buoy- and SAR-derived surface fluxes in the western Weddell Sea during Ice Station Weddell 1992

Cathleen A. Geiger¹

Center for Climatic Research, University of Delaware, Newark, Delaware, USA

Mark R. Drinkwater

Oceans/Ice Unit, European Space Agency, European Space Research and Technology Centre, Science and Applications Department, Noordwijk, Netherlands

Received 29 August 2003; revised 30 November 2004; accepted 28 January 2005; published 7 April 2005.

[1] We examine sea ice kinematics relevant to surface fluxes using ERS-1 synthetic aperture radar (SAR) images coincident with buoys in the western Weddell Sea in austral autumn of 1992. Careful matching of temporal and spatial scales shows that buoy- and SAR-derived velocities differ in root-mean-square error (RMSE) by 0.6 cm s^{-1} and 7.80° in magnitude and direction, respectively. These values represent agreements of 91.3% and 92.7%, respectively, and correspond to instrument uncertainties. Scaling analysis shows that shear matching is best at the smallest scales ($\leq 5 \text{ km}$), while divergence is better represented at scales of 40 km and larger. Sensitivity to error propagation shows lower agreement for divergence (47.4%; $\text{RMSE} = 7.46 \times 10^{-8} \text{ s}^{-1}$), but we find these results sufficient for integrated surface flux comparisons. Using a toy model, we test the effects of aliasing in surface flux determination. The results show that variability associated with storms, ocean tides, inertial oscillations, and other high-frequency forcing affects integrated sea ice growth rates along this continental slope location. Integrated salt and new ice production rates computed from buoys are found to be two times larger than those computed from ERS-1 SAR motion products. We show that these differences in salt and ice production rates result primarily from inadequate temporal resolution of heat flux variability and sea ice divergence. Comparison with other studies shows that the problem is widespread, thereby impacting the modeling of sea ice mass balance and variability. The small-scale processes cited here have significant ramifications for larger scales and the global thermohaline circulation.

Citation: Geiger, C. A., and M. R. Drinkwater (2005), Coincident buoy- and SAR-derived surface fluxes in the western Weddell Sea during Ice Station Weddell 1992, *J. Geophys. Res.*, 110, C04002, doi:10.1029/2003JC002112.

1. Introduction

[2] Deep water formation in the polar regions is the critical pumping mechanism responsible for transporting surface waters to the deepest parts of the global thermohaline circulation. In the Southern Hemisphere, deep water forms dominantly along the Antarctic continental margin, where small-scale coastal shelf/slope processes produce most of the Antarctic Bottom Water (AABW) [Gordon, 1998]. Studies by Carmack [1977], Gill [1973], Foster and Carmack [1976], Gammelsrød *et al.* [1994], Gordon [1998], Whitworth *et al.* [1998], and others confirm this, especially in the Weddell Sea, where 70% of AABW forms

[Carmack, 1977; Rintoul *et al.*, 2001]. Hence there is a definitive connection in the Weddell Sea between small-scale processes and the global circulation.

[3] Numerical models simulate multiscale deep water formation processes using either vertical diffusion and convective adjustment [e.g., Hibler and Bryan, 1987; Mellor and Häkkinen, 1994] or full nonhydrostatic formulations capable of explicitly handling the convective features [e.g., Jones and Marshall, 1993; Marshall *et al.*, 1997]. However, accurate estimates of salt and heat fluxes at the surface boundary are critical inputs in all such models. Timmermann *et al.* [2001] used the Bremerhaven Regional Ice-Ocean Simulations (BRIOS) to show that sea ice production at the boundary is a necessary condition for the development of High-Salinity Shelf Water (HSSW) and deep water formation along the western and southern shelf/slope of the Weddell Sea. Hence the surface interface in realistic models is a complex air/ice/sea boundary from which salt and heat fluxes must be determined with a high degree of accuracy.

¹Now at Snow and Ice Branch, Cold Regions Research and Engineering Laboratory, Environment Research and Development Center, Hanover, New Hampshire, USA.

[4] Sea ice is an insulator working as a “governor” to regulate surface fluxes. Sea ice divergence is the primary kinematic invariant for specifying open water fraction and therefore defines the location of highest salt and heat fluxes. *Eisen and Kottmeier* [2000] demonstrate that high surface fluxes found along the western Weddell Sea are a result of (1) windier and colder atmospheric conditions and (2) highly variable diurnal and semidiurnal tides. Small-scale leads contribute to large area average heat fluxes of 30 W m^{-2} , representing more than 80% of the surface energy transfer for that region. In their estimates, leads contribute to 40% of the annual ice production for the western Weddell Sea. This is three times more ice production than in the central and eastern Weddell, with even higher salt production contribution (60%) caused by high brine rejection rates in the constantly forming new thin ice within leads.

[5] Processes contributing to these high production rates include sea ice inertial oscillations and large ocean tidal velocities interacting with steep topography on the western Weddell shelf break and continental slope. These processes affect net advective transport and therefore influence low-frequency ocean variability. In combination with sea ice, these processes modify sea surface temperature and salinity [*Robertson et al.*, 1998, and references therein]. *Kottmeier and Sellmann* [1996] show that the variability of sea ice divergence over the continental shelves and slopes in the Weddell Sea is controlled to a large extent by the spatial inhomogeneity of ocean tides and inertial motion with spatial scales of 10–100 km. Along the continental slope, sea ice divergence/convergence oscillates around a near-zero mean with a variance of 10^{-6} s^{-1} [*Geiger et al.*, 1998a], which is equivalent to mean open water fractions of 5–10%.

[6] The tidal divergence/convergence oscillations behave like an “ice accordion” [*Foldvik and Gammelsrød*, 1990; *Padman and Kottmeier*, 2000] to cyclically create open water during the divergence phase and then redistribute that new ice onto existing ice floes during the convergence phase. This provides a mechanism for creating more open water and therefore more area for new thin ice to form. Hence this process not only provides a means for producing large amounts of new ice, but a mechanical redistribution for thickening [*Foldvik and Gammelsrød*, 1990] and high ice production through continuous new open water in leads. The results of such ice-building processes are seen in the regional distribution maps of sea ice concentration from Special Sensor Microwave Imager (SSM/I) observations described by *Padman and Kottmeier* [2000, Figure 3], who show that high concentrations (>90%) of sea ice are present most of the time (>90%) along the western and southern slopes of the Weddell Sea, but only rarely is the concentration 100%.

[7] In general, tidal frequency ice velocity and divergence differ from the underlying ocean tidal currents [e.g., *Padman et al.*, 1992] because of differences in spatial scales between the ocean tidal current variability and sea ice. However, in this region, the scales are the same; the ocean tidal divergence variance along the Weddell Sea shelf break from an ocean-only model [*Padman and Kottmeier*, 2000, Plate 3] is 10^{-6} s^{-1} . While there are no coupled ice-ocean tidal models to date for the Antarctic, coupled modeling for the Arctic [*Kowalik and Proshutinsky*, 1994] demonstrates

that ocean tidal frequencies can interact with the divergence and shear of sea ice to enhance surface heat and salt fluxes.

[8] How does one observationally validate and/or numerically assimilate such vast, complex, and intricate processes? Large-scale, high-resolution satellite data is the most comprehensive way to archive and catalogue sea ice features into a form compatible with models. Satellite synthetic aperture radar (SAR) with a spatial resolution as high as 10 m, is sufficient to resolve individual leads. Such active microwave instruments are able to detect high-salinity areas of ice because of their high permittivity, reflectivity, and contrast with the surrounding ice floes [*Drinkwater et al.*, 1991; *Rignot and Drinkwater*, 1994; *Kwok et al.*, 1992, 1995; *Kwok and Cunningham*, 1994]. The fundamental concern is adequate temporal resolution. Polar-orbiting SAR instruments are limited by revisit times (typically 3 days). This means that, relative to the small-scale processes in leads, SAR has sufficient spatial resolution but suboptimal temporal resolution. Conversely, drifting surface buoys have a relatively high temporal resolution (hourly) but are spatially sparse in the field (i.e., low spatial resolution) with episodic deployments.

[9] Another caveat with polar-orbiting satellites is aliasing, which occurs when the satellite revisit time is too long to resolve the frequencies of a specific process [e.g., *Emery and Thomson*, 1997]. *Gloersen* [1995] encountered aliasing when seeking the El Niño–Southern Oscillation (ENSO) signal in sea ice using more than 20 years of SSM/I records. That study identified a 3 year peak ($\sim 0.001 \text{ cpd}$) in sea ice brightness temperature. Regrettably the peak was contaminated with an unknown amount of tidal aliasing caused by 1 day image intervals. This finding limited that study of ENSO responses in the polar regions and discourages others from attempting similar studies, given the orbital configuration of most existing polar-orbiting satellites. *Smith et al.* [2000] found that ERS-1 orbits alias the dominant tidal constituent for the region (K_1) with the annual cycle, while the S_2 tide cannot even be observed because of its Sun-synchronous orbit. The M_2 tide is aliased with the minor N_2 constituent that can be decorrelated with no less than 9 years of data.

[10] One solution is a high-temporal, high-spatial composite or synthesis of buoy and SAR imagery for key regions of interest. From there, surface fluxes can be derived using SAR images coincident with buoy arrays equipped to resolve key properties of sea ice, surface ocean measurements, and surface atmospheric conditions. These regional case studies can then be used to better parameterize surface fluxes in models. In addition to ISW 1992 results reported here, this is an idea that has been partly addressed by later experiments, such as the Surface Heat Budget of the Arctic Ocean (SHEBA) [*Perovich and Elder*, 2002] and the Southern Ocean Global Ocean Ecosystems Dynamics Program (SO GLOBEC) [*Perovich et al.*, 2004]. However, the task remains to create an effective high-temporal, high-spatial buoy-SAR composite. To date, the unsolved problems include the 100 km swath width and orbital constraints of ERS-1 and -2, the limited tape-recording capacity of RADARSAT’s Antarctic wide-swath SAR operations that are outside receiving station range, and the limitation on Antarctic wide-swath coverage on Envisat advanced synthetic aperture radar in its 35 day repeat orbit.

Table 1. SAR Scenes Selected

Scene	Date	Time ^a	Center Location		Orbit	Frame	Buoys
			Longitude, °W	Latitude, °S			
1	19 Feb. 1992	50.1859	53.101	71.414	3111	5697	2
2	21 Feb. 1992	52.4824	53.035	71.587	3144	5103	2
3	22 Feb. 1992	53.1858	53.096	71.413	3154	5697	3
4	25 Feb. 1992	56.1858	52.836	71.525	3197	5697	3
5	27 Feb. 1992	58.4824	53.069	71.576	3230	5103	3
6	2 March 1992	62.1858	53.100	71.414	3283	5697	2
7	4 March 1992	64.4824	53.017	71.589	3316	5103	4
8	10 March 1992	70.4825	53.029	71.589	3402	5103	4
9	11 March 1992	71.1859	53.114	71.422	3412	5697	4
10	11 March 1992	71.1861	54.799	70.698	3412	5715	2
11	14 March 1992	74.1859	53.121	71.416	3455	5697	4
12	14 March 1992	74.1861	54.811	70.693	3455	5715	2

^aTime shown as decimal days of the year, noting that 1992 is a leap year.

[11] In this paper, we focus primarily on the problems associated with coincident buoy and SAR acquisitions. In particular, we consider the following key questions. (1) How well do observed data, specifically buoy- and satellite-derived motion products, compare in the western Weddell Sea along the shelf/slope region where high surface fluxes and resulting deep water formation are important? (2) What are the differences between the products of these two instruments, especially in the computation of sea ice divergence as it relates to the temporal resolution of surface fluxes and new ice growth rates? (3) What physical processes (and associated temporal scales) are responsible for the differences recorded by these two instruments? (4) How do these differences influence the modeling of surface fluxes in this region?

[12] In addressing these questions, the paper proceeds as follows. Section 2 describes the data processing of surface drifting buoys coincident with SAR imagery. Section 3 is a comparison of data products at a common timescale, while section 4 addresses the differences found at each instrument's temporal resolution. In section 5, we investigate these differences with respect to heat flux, new ice growth, and salt flux estimates. Section 6 discusses these results in a larger context, and section 7 summarizes by addressing the overall scientific impact.

2. Data Processing

[13] There is, to date, only one winter field experiment in the western Weddell Sea: Ice Station Weddell (ISW) 1992 [Gordon *et al.*, 1993; Gordon, 1998]. From day 50 to 74 of 1992 during the 5 month ISW field experiment, 12 pre-scheduled ERS-1 SAR image acquisitions, each 100×100 km in size, coincide with a 150×100 km Argos buoy array. Table 1 lists the times and positions of SAR images coincident with the buoys. The orbit of ERS-1 was fixed during the ISW field program in "ice-phase" 3 day, exact repeat orbit, such that, the deployment location of ISW was chosen on the basis of the ERS ground tracks. Thus the satellite ground tracks are fixed in geographical space. As a consequence, all data from exact repeat and ascending and descending crossing orbits were used to maximize the potential revisit opportunities. The main limitation in establishing coincidence is that the buoy array is drifting through the satellite orbit swath frames. A schematic overview of the research area is shown in Figure 1.

2.1. Synthetic Aperture Radar (SAR) Processing

[14] The SAR images are projected onto the polar stereographic Special Sensor Microwave Imager (SSM/I) grid, with 70°S chosen as the reference latitude (plane of no distortion), 0° Greenwich for the reference longitude, and an eccentricity for the Earth's surface shape of $e = 0.08181615$.

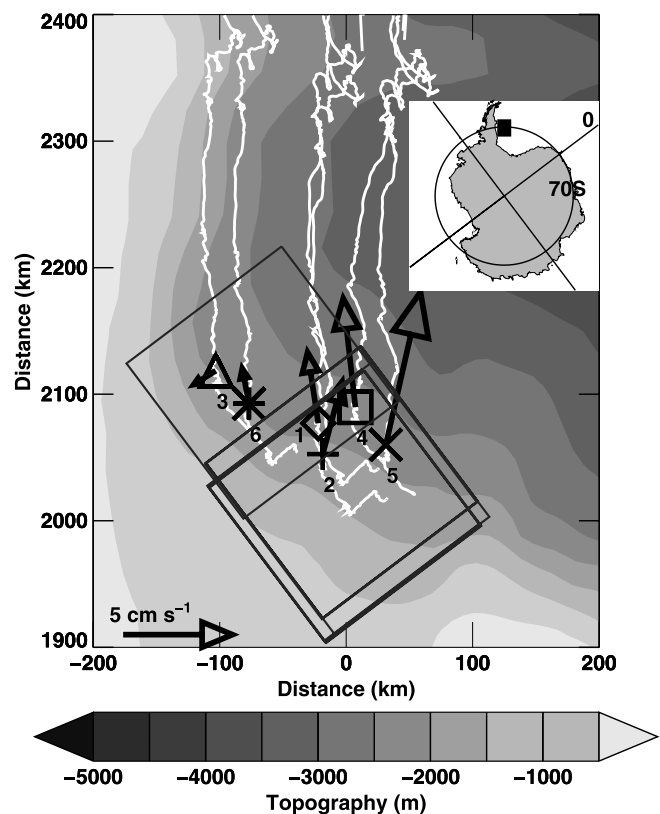


Figure 1. Coincident surface buoy trajectories (white) and synthetic aperture radar (SAR) image footprints (large squares) projected onto the polar stereographic Special Sensor Microwave Imager (SSM/I) grid (see text), with distance relative to north along 53°W . For example, buoy positions (1, camp; 2, Alex; 3, Ed; 4, Brent; 5, Dimitri; 6, Chris (details in Table 2)) and their hourly velocity (vectors) are shown for day 72.7. The insert shows the geographic location, with the small black box exactly matching the research area of the main figure.

Table 2. Buoy Range Selected^a

Buoy ID	Start				End			
	Date	Time ^b	Longitude, °W	Latitude, °S	Date	Time ^b	Longitude, °W	Latitude, °S
GPS (camp) ^c	19 Feb. 1992	50.00	52.351	71.369	16 March 1992	76.00	53.586	70.620
1430 (Alex)	19 Feb. 1992	50.00	52.150	71.582	16 March 1992	76.00	53.485	70.838
1433 (Ed)	21 Feb. 1992	52.08	54.060	71.199	3 March 1992	63.00	54.662	71.204
	4 March 1992	64.08	55.476	70.894	16 March 1992	76.00	55.825	70.306
1431 (Brent)	19 Feb. 1992	50.00	52.354	71.369	1 March 1992	61.00	53.205	71.375
	3 March 1992	63.08	52.261	71.251	16 March 1992	76.00	52.751	70.506
1432 (Dimitri)	19 Feb. 1992	50.00	52.354	71.368	1 March 1992	61.00	53.200	71.376
	3 March 1992	63.08	51.528	71.497	16 March 1992	76.00	52.040	70.737
1435 (Chris)	2 March 1992	62.04	54.824	71.141	16 March 1992	76.00	55.155	70.498

^aBuoy positions are measured using Argos. Buoys with more than one start/end pair were repositioned with helicopter; data were flagged accordingly. Note that buoys Brent and Dimitri are active but on the camp ice floe until March 3.

^bAll times shown as decimal days of the year, noting that 1992 was a leap year.

^cCamp measurements were made using a GPS unit.

Once the images are geocoded, it is necessary to block average to 100 m resolution (8×8 pixel block averaging) to speckle filter the images to minimize intensity errors to ± 1 dB ($>90\%$ confidence interval). Motion vectors for each 100×100 km SAR frame are then resolved as displacements using a nested correlation procedure [Drinkwater, 1998a, 1998b] to characterize 5×5 km spatial patterns composed from 100 m average pixels within a start image. The same pixels are sought automatically in a sequential image with the displaced center of the most highly correlated feature being used to define feature displacement [Drinkwater, 1998a, 1998b]. Individual velocities are then obtained by dividing by the time between each image pair. We assign these vectors to the midpoint in time between images to match them with the buoy information, thereby giving us 10 matched pairs.

[15] The buoys were deployed at the southern end of the continental slope and proceeded northward, closely tracking along 53° W longitude parallel to local bathymetry (parallel to the continental shelf break and slope) as illustrated in Figure 1. For these reasons, the motion vectors are also computed on an SSM/I grid oriented relative to 53° W, as are all figures (except Figures 3 and 9, which are oriented relative to Greenwich).

2.2. Buoy Processing

[16] The buoy data used here are a subset of a larger study described by Geiger *et al.* [1998a]. The deployment of the buoy array began on 19 February (day 50), with some sporadic relocation of the buoys using a helicopter until 4 March (day 64) as noted in Table 2. Buoy position was determined via Argos about eight times a day and nearly hourly at the camp using the global positioning system (GPS).

[17] Latitude and longitude positions of the buoys were transformed to x , y positions on the SSM/I grid, with orientation relative to north along longitude 53° W. Data gaps of 3 days or less were linearly interpolated to hourly positions, with longer gaps flagged as undefined. Data quality control in the form of a simple forward difference velocity was used to flag suspect sections of the trajectory with a threshold velocity and velocity change of 50 and 20 cm s^{-1} , respectively. The signal was linearly interpolated, with a 10% reflected signal added to the edges in preparation for filtering. Because the ISW region is

known to experience strong tidal forcing, the buoy x , y positions were filtered with a 9 hour Butterworth four-pole low-pass filter (an infinite impulse response filter) to minimize high-frequency noise while still retaining nearly all of the tidal signal [Geiger *et al.*, 1998a]. The 9 hour filter's stop band begins at the associated frequency of 2.67 cycles d^{-1} , with 85% of the signal still retained in the pass band frequencies associated with the highest tidal frequencies (around two cycles per day).

[18] Centered differencing of interpolated, filtered positions is used to compute velocity, with final quality controls, including prefiltered flags and checks of extreme velocities, on the final result. These "cleaned" position and velocity results were used for the remainder of the study, with flagged data handled as undefined information. Two time step intervals were used for the buoy velocity. The first is a centered differencing based on hourly buoy positions such that $u(t) = [x(t + \Delta t) - x(t - \Delta t)]/2\Delta t$ where Δt is 1 hour. The second method is used to process the buoy data to the same temporal resolution as the SAR images. We do this using a variable sliding-time-window-centered differencing scheme such that $u(t) = [x(t + \Delta t/2) - x(t - \Delta t/2)]/\Delta t$ where Δt is the time interval between SAR images relative to the centered time t . As an example, the buoy velocity at time t between SAR images 1 and 2 (Table 1) is computed as a displacement based on 2.2965 days, but between SAR image 2 and 3 it is based on 0.7034 days. The resulting velocity is piecewise smooth and can be analyzed in segments. This buoy velocity product will be referred to here as the aliased buoy data because it is temporally smoothed beyond the timescales of some processes we wish to examine.

2.3. Local Drift and Deformation

[19] Buoy arrays are sparse in number but provide reasonable deterministic estimates of local drift and deformation when computed in groups of three, provided the array aspect ratio does not become extreme. Furthermore, estimates can be quality controlled with confidence intervals when clustered in groups of six buoys or more [Thorndike, 1986; Geiger *et al.*, 2000]. During the coincident SAR phase of ISW, there were fewer than six buoys, making it impossible to compute confidence intervals on resulting strain rate estimates. However, multiple linear regression was still a viable means of computing linear estimates of sea

ice deformation when three to five buoys were available. Using multiple linear regression [e.g., *Geiger et al.*, 1998a; *Hines and Montgomery*, 1990], we solve for the unknowns of local velocity $(v_i)_0$ and associated local derivatives $(\partial v_i / \partial x_j)_0$ given known particle velocities $(v_i)_n$ and their distance from a chosen local point $\Delta(x_i)_n = (x_i)_n - (x_i)_0$. Velocity can be computed using a Taylor expansion about a local point of interest $(x_i)_0$ such that

$$(v_i)_n = (v_i)_0 + \left(\frac{\partial v_i}{\partial x_j}\right)_0 (\Delta x_j)_n + \frac{1}{2} \left(\frac{\partial^2 v_i}{\partial x_j \partial x_k}\right)_0 (\Delta x_j \Delta x_k)_n + \dots, \quad (1)$$

where repeated indices sum, $i, j, k = 1, 2, \dots$ spatial components, $n = 1, 2, \dots$ is indexing known particles (i.e., buoys and SAR products), and the index 0 identifies the local point of interest from which $(x_i)_n$ is measured. Velocity magnitude, velocity direction, and the strain rate invariants of divergence and maximum shear follow from this solution as described by *Geiger et al.* [2000].

[20] Local drift and deformation of a buoy array is computed using this multiple linear regression method with the geometric center of the buoy array chosen as the local point. For SAR-derived motion vectors, we compute local drift and deformation relative to the geometric center of the buoy array assuming a range of inclusion radii from 5 to 75 km to determine the scale at which the two data sets best match [*Geiger et al.*, 2000]. Seven coincident deformation arrays were constructed based on sequential SAR pairs where three or more buoys are available (Table 1).

[21] Statistical analysis such as signal-to-noise and confidence intervals for the divergence results are not possible for this part of the buoy time series because so few buoys were available at this time. However, results from the original study by *Geiger et al.* [1998a, Table 3] show average signal-to-noise ratios of nearly 20:1 and 2:1 for velocity and deformation components, respectively. The deformation signals have significant peaks found at the storm, diurnal, and semidiurnal frequencies. With this knowledge, we focus the analysis in this paper on the significant peak frequencies found in the buoy signals of earlier work.

2.4. Statistics

[22] To determine an optimal scale to sample satellite-derived motion vectors compared to buoy arrays, we utilize the root-mean-square error (RMSE) between two data sets [*Geiger et al.*, 1998a, 2000], specifically,

$$\text{RMSE} = \sqrt{\frac{1}{K} \sum_{k=1}^K \sum_{n=1}^N (S_{nk}^{(1)} - S_{nk}^{(2)})^2}, \quad (2)$$

where $N = 1$ for the RMSE between scalar quantities of two data sets ($S^{(1)}$ and $S^{(2)}$) indexed as sequential data in time by k for $1 \leq k \leq K$, and $N > 1$ to index between multiple components of two data sets (i.e., velocity vector $n = 1, 2$; first-order velocity derivatives $n = 1, 2, 3, 4$).

[23] A second useful statistic is the index of agreement d developed by *Willmott et al.* [1985] as a practical alternative to correlation since it scales with the magnitude of the variables through its retention of mean information. For

equally weighted observed (\mathbf{o}_k) and predicted (\mathbf{p}_k) data points, this measure is formulated as

$$d = 1 - \left[\sum_{k=1}^K |\mathbf{d}_k| \right] \left[\sum_{k=1}^K (|\mathbf{p}_k - \bar{\mathbf{o}}| + |\mathbf{o}_k - \bar{\mathbf{o}}|) \right]^{-1}, \quad (3)$$

where K is again, the number of data points for either scalar or vector quantities, $\mathbf{d}_k = \mathbf{p}_k - \mathbf{o}_k$ is the difference between predicted and observed, $\bar{\mathbf{o}} = (\sum_{k=1}^K \mathbf{o}_k) / K$ is the mean of the observed.

2.5. Data Uncertainties

[24] The temporal uncertainties of SAR and buoys are assumed to be negligible, as both involve precise time stamps in their satellite telemetry. Hence the primary source of measurement error is spatial uncertainty.

[25] For Argos buoys, the position uncertainty or geolocation error is the primary error at a value of about 350 m. Since all velocity calculations are done with centered differencing, the position uncertainty from the buoys x'_b (prime denotes uncertainty, b denotes buoy) propagates to a velocity uncertainty v'_b using the relationship $v'_b = x'_b / (\sqrt{2} \Delta t_{\text{sampled}})$. With the data collected roughly every 3 hours from the buoys, the interpolated hourly time series has a velocity uncertainty of 2.3 cm s^{-1} . When computed at the various time intervals in the aliased form, this uncertainty reduces to anywhere from 0.10 to 0.41 cm s^{-1} for 3 day and 0.7 day interval, respectively (0.7 days is the shortest SAR pair time interval). The one exception is the GPS located at the camp, where measurements were taken nearly hourly. The GPS is rated with a geolocation error on the order of 30 m. Propagating this error, the camp has a velocity uncertainty of 0.59 cm s^{-1} for hourly data.

[26] According to *Holt et al.* [1992] and *Lindsay and Stern* [2003], the variance of the displacement error between SAR pairs for ERS-1 SAR is about 330 m, resulting from a combination of geolocation (100 m) and feature identification (300 m) errors. As this error is already propagated to displacement $\delta x'_s$, propagating it further to velocity will make it scale inversely with the time interval, or $v'_s = \delta x'_s / (2\Delta t)$. This corresponds to velocity uncertainties from 0.06 to 0.27 cm s^{-1} for 3 day and 0.7 day, respectively. Conservatively taking the largest uncertainty that both instruments have in common, we anticipate combined velocity errors $\sim 0.48 \text{ cm s}^{-1}$.

[27] Using all available data, scatter plots in Figure 2 show an RMSE of 0.60 cm s^{-1} for velocity magnitude and 7.8° for direction. If we discount the single outlier in parentheses in Figure 2a, the RMSE reduces to 0.47 cm s^{-1} (92.6% agreement), which is close to the estimated instrument uncertainty.

3. Similarities Between Buoys and SAR

[28] The 25 day period from 19 February (day 50) to 14 March (day 74) is the only time during ISW when Argos buoys coincide with closely spaced SAR pairs (Table 1). The motion vectors compare well (Figures 2 and 3) when the buoy velocities are processed to the same time intervals as corresponding SAR pairs. We note increased magnitude and spatial variability in Figures 3b and 3h corresponding to the shortest time intervals between SAR pairs (0.7 days).

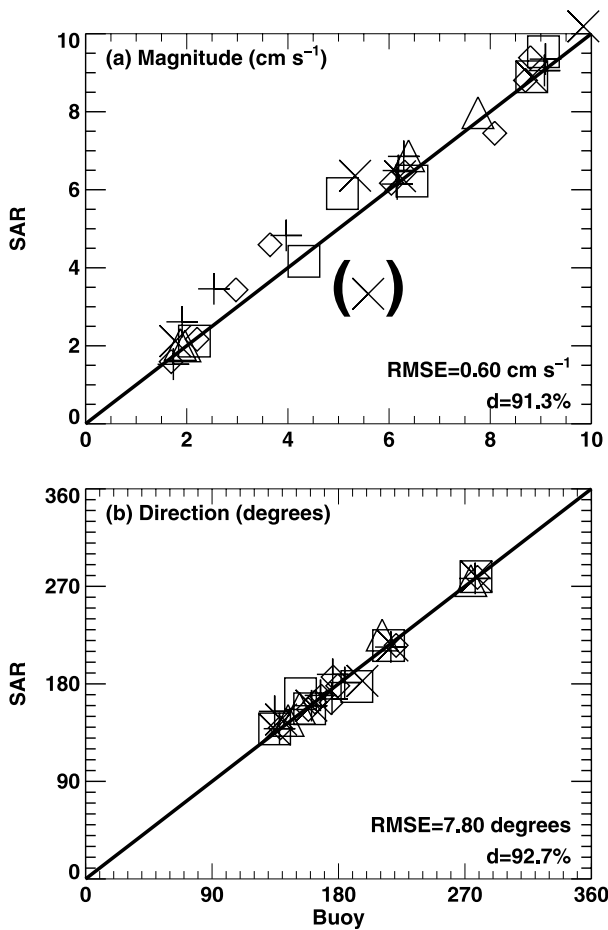


Figure 2. Scatterplots between closest temporal and spatial aliased buoy- and SAR-derived motion products of velocity (a) magnitude and (b) direction. A total of 38 matches are shown with corresponding root-mean-square error (RMSE) and index of agreement d . Symbols correspond to those in Figure 1. Exclusion of the outlier in parentheses reduces the RMSE to 0.47 cm s^{-1} (92.6% agreement) for magnitude.

Despite the limited samples, we contend that this distinction is real.

[29] Following the method of *Geiger et al.* [2000], minimization of RMSE between buoy and satellite-derived motion products helps characterize scales of motion. Despite the limited number of samples (only seven), a systematic pattern of scales results (Figure 4). For velocity, SAR-derived motion products and buoy arrays agree to within 95% (based on the index of agreement) at scales of 5 km, with a slight linear reduction to 87% at scales of 75 km.

[30] Deformation variables are more sensitive than velocity to spatial scales. The shear values have good agreement (84%) at the 5 km search radius (or inclusion radius) but decrease rapidly to 50% agreement at a scale of 35 km and thereafter fluctuate about that value. The inverse is true for divergence, which shows low agreement at the 5 km scale but quickly meets the same 50% agreement at about the same scale as shear (40 km). The agreement based on all four velocity gradient terms (i.e., $\partial u_i / \partial x_j$) fluctuates about 50% agreement over all scales tested with this data set. The

scale response of divergence and shear makes intuitive sense, since shear patterns typically manifest themselves as long and narrow cracks while divergence/convergence typically manifests itself at a larger scale in the form of isotropic relaxation/compression of ice stresses and opening/closing of the floe field. On the basis of earlier works [*Geiger et al.*, 1998a, 1998b, 2000], this level of agreement

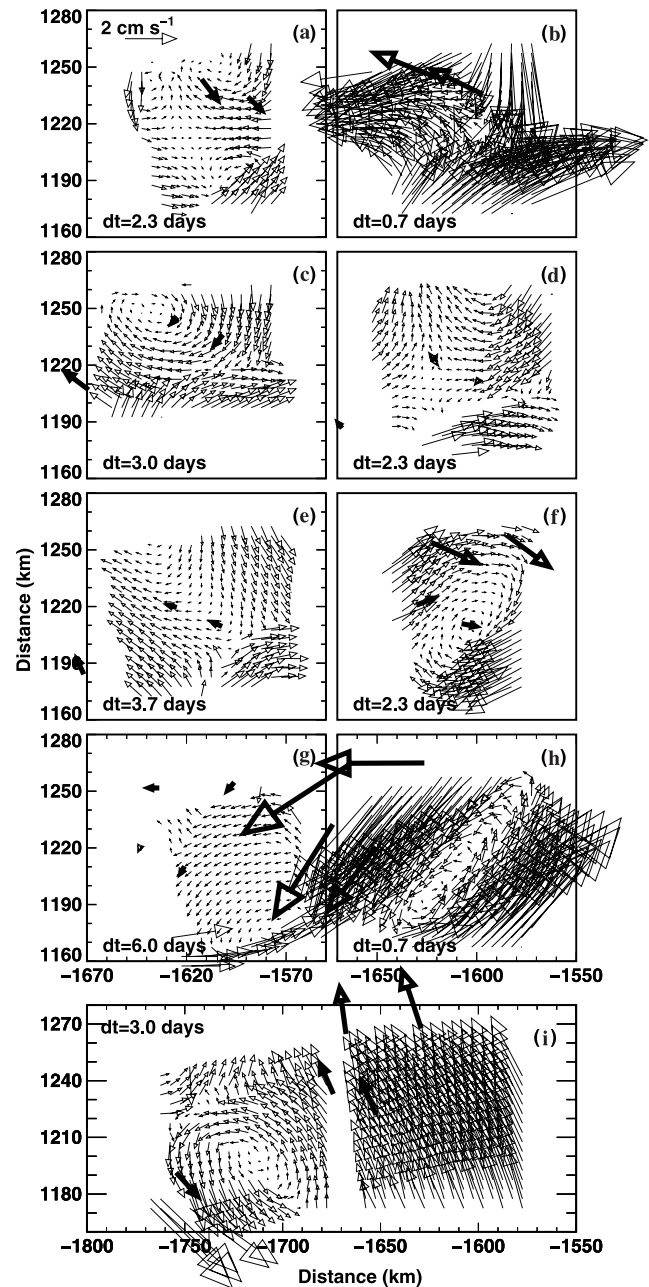


Figure 3. Relative velocity vectors (mean removed) from SAR pairs (Table 1) shown on an SSM/I grid (km) orientated relative to Greenwich. Note that the last two pairs are included in Figure 3i. Superimposed is the distribution of coincident buoys. The time separation dt between pairs is applied to the buoys with the same mean SAR motion removed. All panels are scaled relative to the reference vector in Figure 3a.

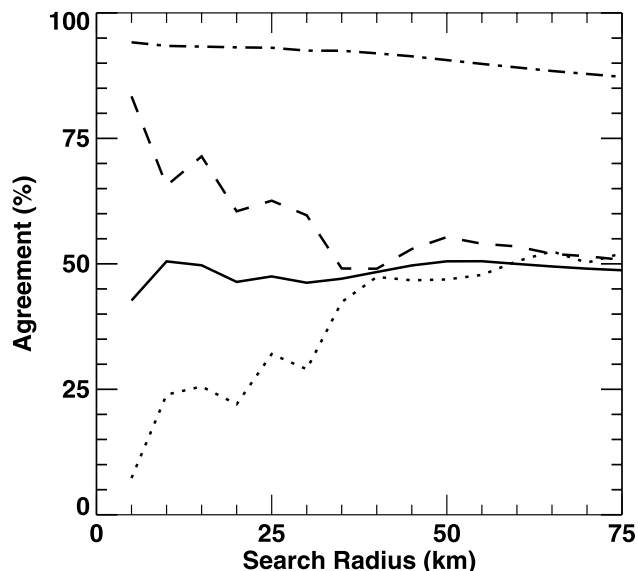


Figure 4. Agreement (see text) between buoy array estimates of local velocity (dash-dotted line), invariant shear (dashed line), divergence (dotted line), and deformation components (solid line) and corresponding SAR-derived products at various search radii. Three or more buoys were in close proximity to SAR image pairs seven times (Table 1), with coincident SAR motion vectors collected within the chosen search radii relative to the buoy array geometric center (details in text).

between buoy deformation variables with either models or images is the maximum found to date.

[31] Since divergence is the critical variable for surface fluxes, Figure 5 shows a scatter plot comparing SAR-derived divergence using a 40 km inclusion radius and aliased buoy results. Following earlier uncertainty estimates, divergence uncertainty D' can be expressed as a function of velocity uncertainty $D' = \sqrt{2} v'/L$, where L is the size of the arrays (~ 55 km and ~ 80 km for buoy and SAR (inclusion radius $\times 2$), respectively). Applying this relationship to the uncertainties presented in section 2 (velocity uncertainty for buoys of 0.41 cm s^{-1} and for SAR of 0.27 cm s^{-1}), we arrive at an upper estimate for divergence uncertainty of 10.5 and 4.8×10^{-8} s^{-1} , respectively. These estimates are above and below, respectively, the RMSE found from the seven coincident divergence events in Figure 5 (7.46×10^{-8} s^{-1}).

[32] The range of SAR-derived divergence tends to be within $\pm 10 \times 10^{-8}$ s^{-1} , while the buoy results are within $\pm 15 \times 10^{-8}$ s^{-1} . This difference is at the level of the noise in this plot. However, this difference will resurface in section 5 during the estimation of surface fluxes. Considering this range as an estimate of the signal and RMSE between the two data sets as an estimate of the noise, we compute signal-to-noise ratios of 2:1 for the buoys (i.e., $15/7.46$), which agrees with results found in the larger study reported by Geiger *et al.* [1998a].

[33] Despite the limited case, the outcome of these few points highlights the sensitivity of mesoscale sea ice deformation to coupled spatiotemporal scales. A similar sensitivity was found in buoy comparisons by Geiger *et al.*

[2000] and Geiger and Drinkwater [2001]. We therefore hypothesize that the sensitivity demonstrated here is realistic and that the propagation of geolocation/position uncertainty is the main contributor to the scatter.

4. Differences Between Buoys and SAR

[34] In the last section, buoy velocities processed to SAR pair time intervals were shown to compare with SAR-derived motion products to within instrument accuracy when temporal and spatial scales were carefully matched. In this section, we emphasize their differences by examining them at their respective temporal resolution. To illustrate these differences, we use the hourly GPS readings taken at the camp and compare these results with image pairs from ERS-1 SAR. Despite the short time sequence, the coincident period covers the passage of a large storm recorded by buoy instruments and highlighted in Figure 6.

[35] Figure 7a shows how well the piecewise smooth aliased buoy velocities match the SAR-derived motion vectors, as demonstrated in the last section. We also see from the hourly camp velocities that this smoothing process eliminates important high-frequency information, including strong semidiurnal and diurnal tidal activity, inertial oscillations, and other motion at periods shorter than 1 day (hereafter referred to as subdaily events) as described by Levine *et al.* [1997] and Geiger *et al.* [1998a, 1998b]. Breaking down each of these signals using a one-dimensional wavelet transform, Figures 7b–7d show the spectra of these three signals as periodograms. The lower two panels show similar patterns with the aliased GPS camp time series (Figure 7c), showing more high-frequency (short-period) signal during times when the camp motion changed the most.

[36] The most revealing signal (Figure 7b) is the hourly camp data, which include strong amplitudes near 0.5 and 1

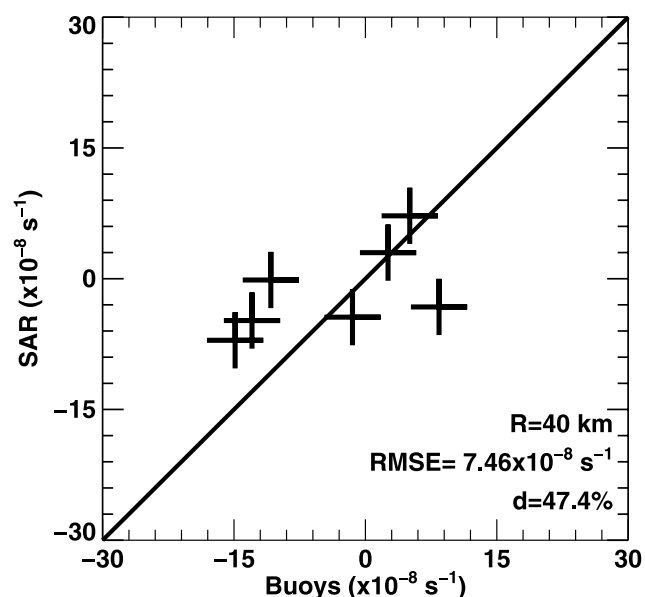


Figure 5. Scatterplot comparing buoy- and SAR-derived divergence using the SAR search radius R of 40 km based on results in Figure 4. Corresponding statistics of RMSE and index of agreement d are also provided.

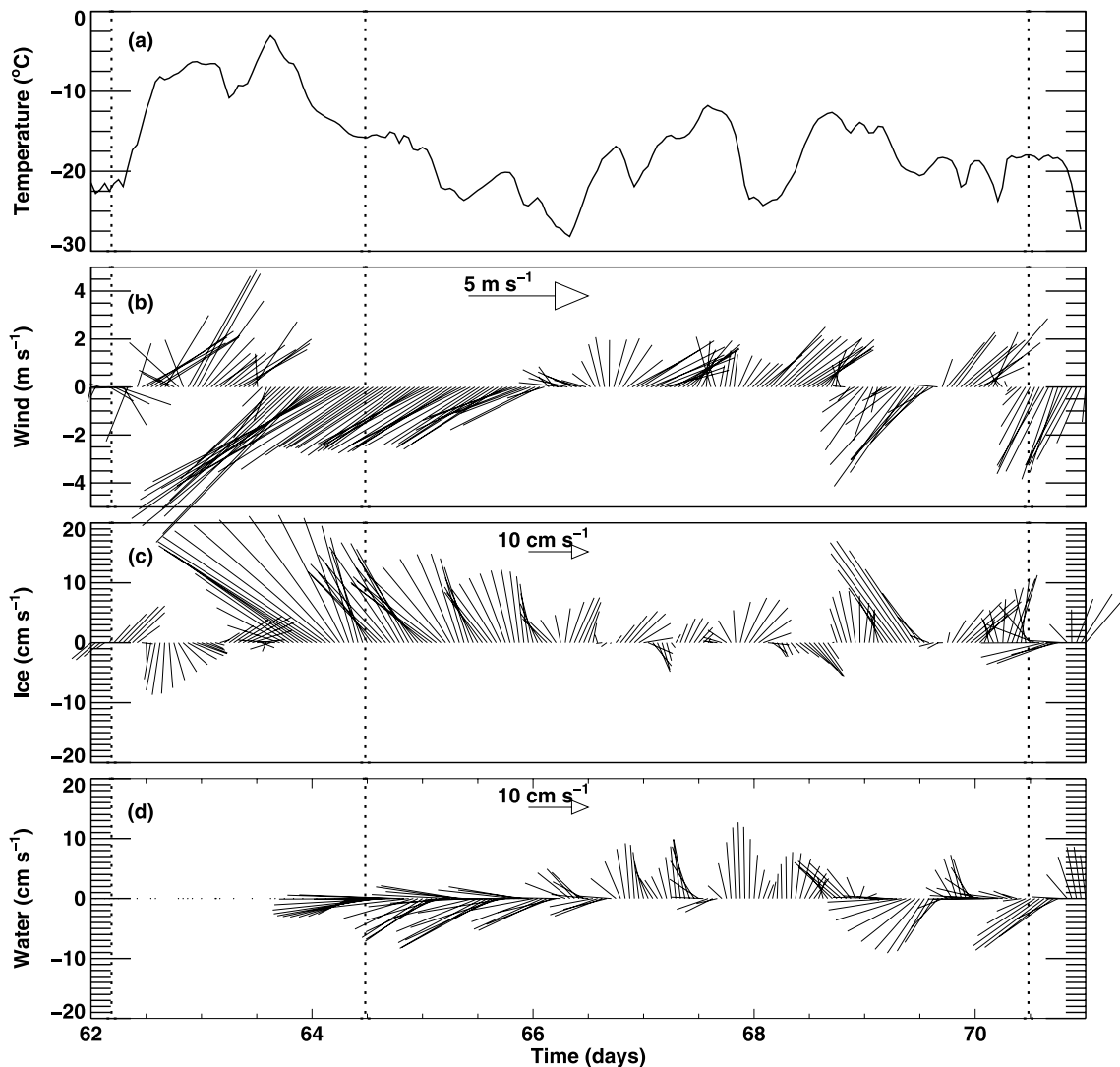


Figure 6. In situ observations through an early austral autumn storm. (a) Air temperature observed at site Chris. (b) Surface winds from site Chris, with north oriented upward on the page. (c, d) Camp ice motion and 25 m ocean current, respectively, with north also oriented upward. Vertical dashed lines indicate SAR acquisition times.

day periods that must be, mostly or at least substantially, due to inertial oscillation and semidiurnal and diurnal tides in this area [Levine *et al.*, 1997; Geiger *et al.*, 1998a, 1998b; Robertson *et al.*, 1998; Padman and Kottmeier, 2000]. Also, centered on day 63.5, a strong 5 day signal corresponds to the storm referenced earlier (Figure 6). This signal coincides with increased amplitudes at the 1 day period. This coincidence of signals suggests the possibility of strong nonlinear mechanical ice/ice interaction. Figure 7 shows that the ice motion is oriented northwest at the peak of the storm. The most rapid change in velocity at this time is in the negative x direction (i.e., perpendicular to the continental shelf break), suggesting a rapid spatial change of tidal currents associated with changing bottom topography. As hypothesized by Padman and Kottmeier [2000], the source for this coupling between tides and storm in the ice drift signal must be nonlinear ice mechanics.

[37] While this is the only storm during the coincident SAR/buoy period, 100+ days of ice drift were recorded at

the camp (days of year 50 to 150+). Querying longer records, two similar periodogram features are found (not shown) near days 80 and 120, when air pressure and wind were changing during the storms. The direction of these storms, the increased compactness of the ice, and the change in ice composition produced less of a pronounced cascade pattern in the periodograms relative to the one shown in Figure 7. Hence Figure 7 is the best illustration, from the entire ISW experiment, of strong nonlinear ice responses in the form of cross-slope velocity amplitude increases, during storm tidal events.

5. Impact on Surface Flux Estimates

[38] In this section, we quantify the differences found in the previous section by examining the impact on new ice production. The overall goal of this paper is to ascertain the significance of different temporal resolutions in buoy- and SAR-derived products. There are prototype models that

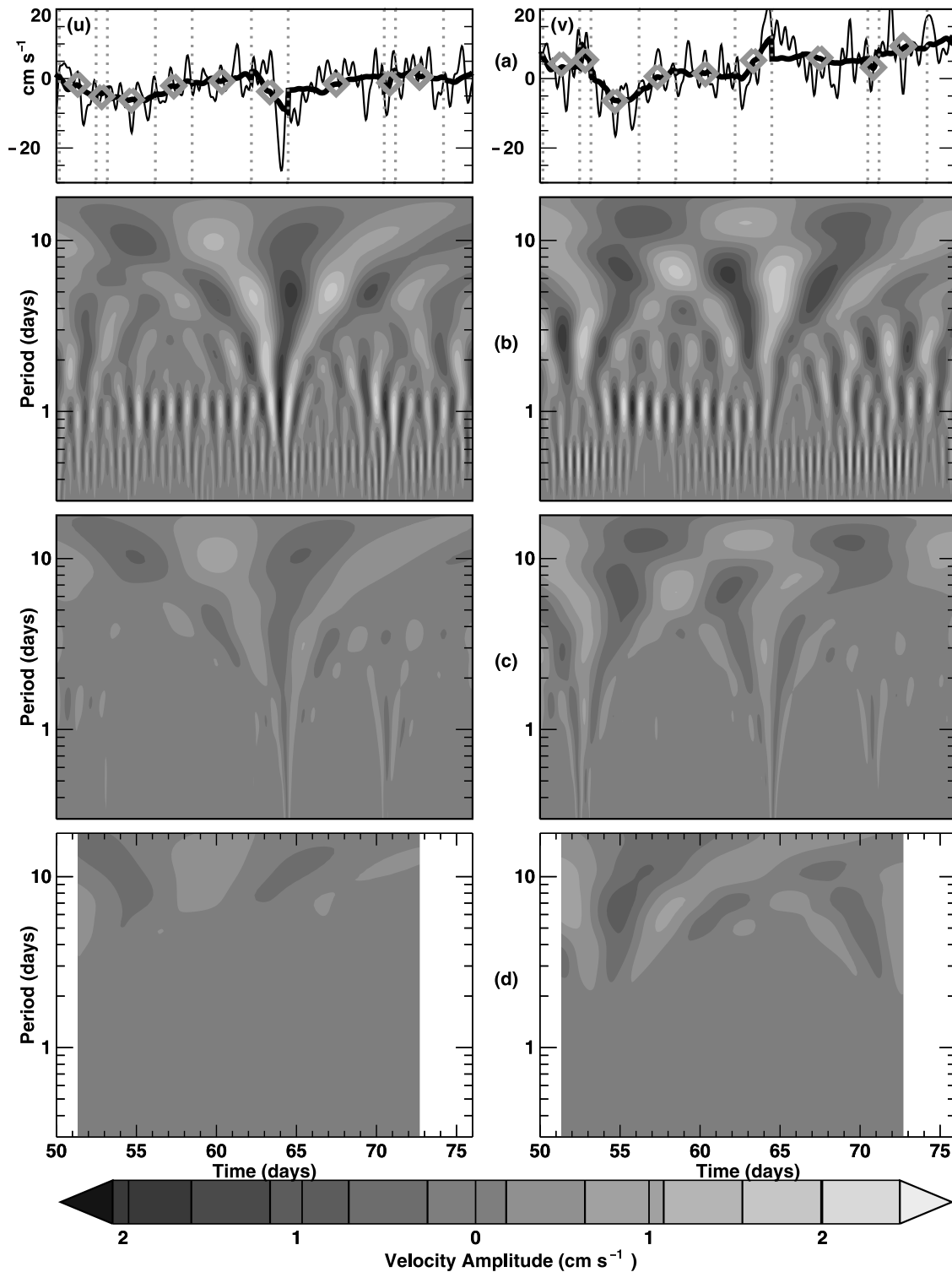


Figure 7. (a) Time series and (b–d) wavelet analysis of velocity components ((left) u and (right) v) from hourly buoy time series at the camp (thin line), aliased buoy time series (bold line), and the closest SAR motion vector (diamonds), with dotted vertical lines at SAR acquisition times. Spectrogram contours using the Morlet wavelet transform are plotted for the hourly buoy time series (Figure 7b), the aliased buoy times series (Figure 7c), and the closest SAR vector time series linearly interpolated (Figure 7d). See color version of this figure at back of this issue.

characterize small-scale lead/polynya processes using a fetch and an active vertical region of freezing called a “collection depth” [e.g., Pease, 1987] based on detailed field measurements from a specific lead or polynya. However, our data are not comprehensive enough to model lead processes in such detail. Likewise, climate, large-scale, and mesoscale models are still in the experimental stage of resolving “lead-type” structures [e.g., Hibler and Schulson, 2000] and therefore lack any parameterizations for describing processes like fetch or collection depth.

[39] Crafting a simple “toy” numerical experiment, we consider small-scale open water areas the same way most larger-scale models do (i.e., as stochastic subgrid-scale events). The exercise focuses on surface flux estimates under the same thermodynamic conditions but under different temporal resolution. The simple bulk formulas are therefore sufficient to address this issue. We want to incorporate remotely sensed information into models in a form that parameterizes leads but, at the same time, identifies the limitations of such parameterizations as a function of temporal resolution. As this is a limited case study, we also wish to check our results relative to other studies. We therefore choose a bulk thermodynamic formulation similar to that described in the 1992–1994 polynya study [Markus *et al.*, 1998] (hereinafter referred to as M98) since they compute surface fluxes using remotely sensed data (SSM/I) and model-based bulk formulations. Their study has the advantage that it also occurs in the same geographic region and overlaps in time with this study.

5.1. Estimate of Surface Heat Flux

[40] In the mesoscale to large scale, ice and salt production at the air/sea interface in polar regions is determined by a surface energy balance using bulk formulas. For open water and thin ice, these formulas are based on inputs of time and position; air properties including temperature, wind velocity, relative humidity (or dew point), and cloud cover; ocean heat flux; and the surface properties of temperature and albedo. Most sea ice models use the bulk formulas by Maykut [1986] or Parkinson and Washington [1979]. Adaptation of these formulas from Hibler [1979] and Geiger *et al.* [1997] describe a surface energy balance

$$H_i = H_s + H_l + Q_{lu} + Q_{bb} + Q_s + F_w + F_{ri}, \quad (4)$$

where H_i is the amount of heat gained or lost at the air/sea interface, H_s is sensible heat flux, H_l is latent heat flux, Q_{lu} is incoming longwave radiation, Q_{bb} is outgoing longwave (blackbody) radiation, Q_s is incoming shortwave radiation, F_w is ocean heat flux, and (when the ice is thick) F_{ri} is the radiation trapped/absorbed in the ice, all in units of W m^{-2} . A negative heat flux at the surface indicates heat loss and therefore reduced surface temperature or freezing to form ice.

[41] In situ data from meteorological instruments on the buoys provide hourly readings of air temperature and wind velocity (Figures 6a and 6b). The air temperature during the period of interest (Figure 6a) is consistently below freezing, so we assume that any open water should be at the freezing point. No in situ humidity data were available, but qualitative field observations (S. Ackley, personal communication, 1993) suggest that, when the winds are blowing from the

sea (compass wind directions from -45° to 135°), the relative humidity is high, while winds off the ice shelves are very dry. On the basis of sensitivity studies by Geiger *et al.* [1997], relative humidities of 90% and 40%, respective to the above wind directions, yield model results in good agreement with observations, so we use those quantities here. Albedo is chosen as a constant (after Hibler [1979]) of 0.1 for open water to very thin ice and a cloud cover of 80% based on typical weather conditions during the time of the experiment. An oceanic heat flux of 7 W m^{-2} is chosen based on measurements computed by Lytle and Ackley [1996] using ISW field data. Since our interest is in thin ice and open water, we set F_{ri} equal to zero.

[42] Once the heat flux H_i at the air/sea interface is calculated, we compute new ice production following M98 using

$$G_i = \frac{-H_i}{\rho_i L_f}, \quad (5)$$

where G_i is the rate of ice growth (m s^{-1}) solved as a function of the surface heat flux (H_i), the density of the ice ($\rho_i = 950 \text{ kg m}^{-3}$ after Pease [1987]), and the latent heat of fusion ($L_f = 3.34 \times 10^5 \text{ J kg}^{-1}$).

[43] Salt production is computed as per M98 for direct comparison with that study as

$$S_f = \rho_i G_i \Delta t (s_w - s_i), \quad (6)$$

where S_f is the amount of salt released in kilograms, Δt is the time over which the ice production takes place, A is the area of open water (m^2), and s_w and s_i are the salinities of the water column and the ice, respectively. Under the same assumptions as M98 (after Martin and Kaufmann [1981]), this relationship reduces to the simple formulation $s_i = 0.31 s_w$, with the salinity in the water column set at 34.45 as reported by Gordon [1998] during ISW. Given the depth of the water column (2250 m) and its location (on the continental slope with direct access to the deep basin), we do not include the salt feedback described by M98 but instead assume that any salt produced is mixed and advected away. Given the absence of the salt feedback process, ice and salt production differ by a constant offset for this study as seen in Figure 8c.

5.2. Parameterization of Open Water

[44] The remaining unknown is an estimate of open water area (A), which is the product of a given area (km^2) and open water fraction (%). We compute the open water fraction directly from a SAR image by identifying open water pixels within a given image [Drinkwater, 1998a, 1998b]. However, we also wish to know the amount of open water at each buoy time and each midpoint time between images. At these times we compute

$$O_{\text{tot}} = O_{\text{ref}} + O_{\text{therm}} + O_{\text{kin}}, \quad (7)$$

where O_{tot} is the total open water fraction (%) at any time t , O_{ref} is the open water fraction relative to some absolute reference at some time t_0 , O_{therm} is the amount of open water created by thermodynamic processes between reference times, and O_{kin} is the amount due to kinematic motion.

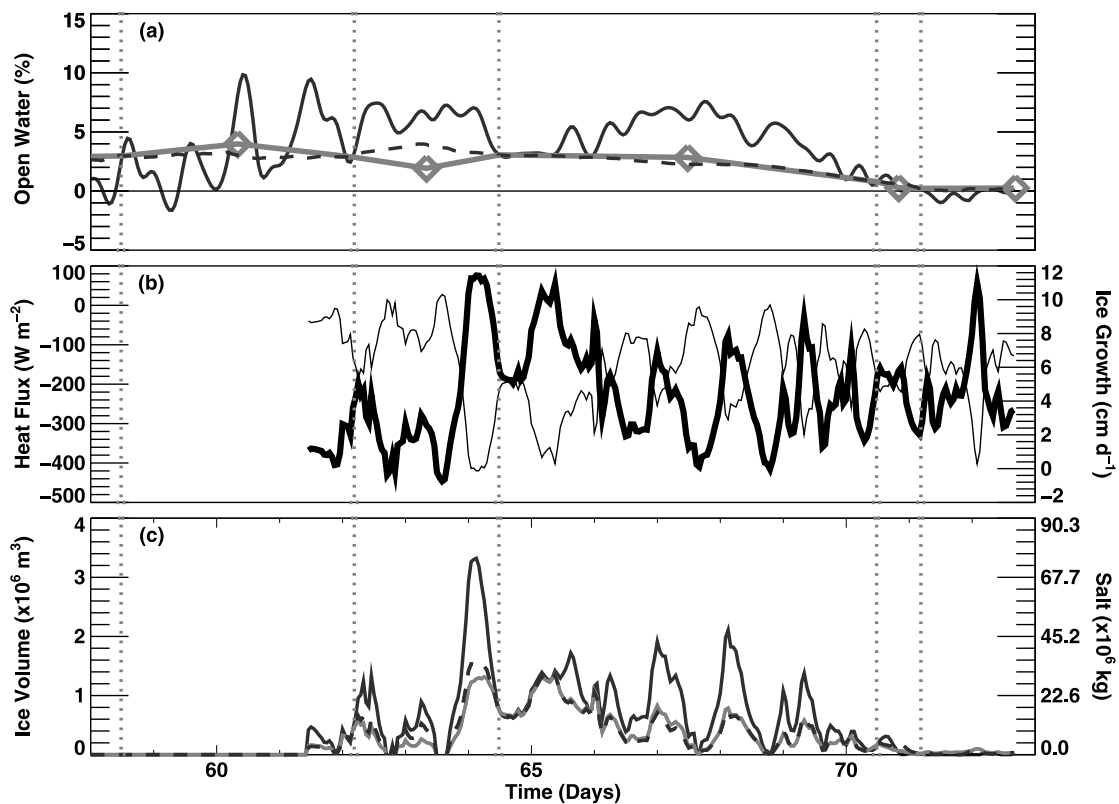


Figure 8. Surface flux estimates using buoy- and SAR-derived motion products, in situ meteorological measurements, and a bulk formula model. (a) Open water fraction from 9 hour low-pass filter hourly buoy positions (solid line), coincident SAR (shaded line with diamonds), and aliased buoy results (dashed line) calibrated as described in the text. SAR acquisition times are denoted by vertical dashed lines. (b) Surface heat flux (thin line) and resulting ice production over open water (bold line) based on the bulk formula model. (c) Sea ice growth (left axis) over open water fraction, using the same line styles as in Figure 8a. Equivalent salt production (along right axis) is scaled to match the ice volume results.

[45] Integrating divergence (s^{-1}) over a given time interval provides changes in open water fraction due to mechanical processes and therefore O_{kin} . We obtain the remaining two terms via an assumed linear fit, namely,

$$O_{ref} + O_{therm} = b + mt. \quad (8)$$

Here we assume that an offset ($O_{ref} = b$) exists between the relative open water fraction computed from O_{kin} and the absolute open water fraction computed from a SAR image. Applying only O_{ref} and O_{kin} gives piecewise smooth results with discontinuities at each image time. Introducing a slope term mt between images removes the discontinuity, thereby creating a continuous function for open water that is physically based and mathematically complete. By process of elimination the slope m represents average changes in thermodynamic processes between images (i.e., $O_{therm} = mt$).

5.3. Estimate of Salt and New Ice Production

[46] Integration of divergence over time provides a reasonable estimate of the open water fraction based on mechanical processes. Using equation (7) we account for mechanical opening/closing, initial open water fraction, and a linear slope adjustment to calibrate the time series. Once calibrated, the open water fraction (Figure 8a) scales com-

parably for buoy and SAR data despite the different time intervals. The biggest difference is the higher open water fraction in the high-frequency buoy signal between SAR images on days 62 and 71. The fact that the aliased buoy signal so closely follows the SAR results in Figure 8a gives us confidence that uncertainties in divergence determination are not significantly large compared to the time sampling issues we wish to focus on.

[47] Because these measurements coincide with the deployment phase of the ISW project, meteorological stations were operational only partway through the SAR acquisition campaign. Hence there are only 12 days when SAR images, buoy positions, and in situ meteorological data all coincide, as shown in Figures 8b–8c. The overlap period is fortuitous, as it includes the storm discussed earlier (Figures 6 and 7). On the basis of the bulk thermodynamic formula described earlier, the average open water new ice growth rate during this period is 4.3 cm d^{-1} (Figure 8b).

[48] Looking carefully at the heat flux and ice production rates based on hourly observations, we see time segments when a large open water fraction coincides with high surface heat fluxes (primarily as a result of high wind speeds and/or low temperatures, Figure 6). These combined environmental conditions result in the highest ice and salt production rates, as noted in the production estimates computed using the fully sampled buoy record (Figure 8c).

Table 3. Comparison During Experiment

Property	<i>Melnikov</i> [1995]	This Study
Air temperature, °C	−22 to −31	−3 to −29
Water salinity, psu	34.4	34.45 [<i>Gordon</i> , 1998]
Water temperature, °C	−1.86	−1.88 [<i>Gordon</i> , 1998]
Ice salinity, psu	13–19	10.68 [<i>Markus et al.</i> , 1998]
Brine salinity, psu	40–120	...
Mean new ice growth, cm h ^{−1}	0.38; <10 cm 0.13; >10 cm	0.24; $T < -22^{\circ}\text{C}$ 0.18; all temperatures (T)
New ice growth rate, cm h ^{−1}	−0.13–0.56	−0.03–0.48
Median growth rate, cm d ^{−1}	5.2	5.4

Note, however, that the SAR results and the aliased buoy records are too intermittent to resolve these large ice and salt production bursts.

[49] The period between days 64.5 and 65.5 is fortuitous, with exceptional agreement between all production estimates as a result of a relatively constant open water fraction just after the SAR image taken on day 64.5 (Figure 8a). That short window of agreement demonstrates the potential for spaceborne flux estimates given sufficiently higher sampling rates and/or synthesis techniques involving both buoys and imagery. These results predict improvements for flux measurements with Advanced Microwave Scanning Radiometer–E (AMSR-E) over RADARSAT because of the higher (daily) repeat orbit rate of AMSR-E despite the lower spatial resolution.

[50] When we integrate the flux rates over the 12 day time period, we get ice (salt) production rates of 99.90 (2256), 103.80 (2327), and $179.30 \times 10^6 \text{ m}^3$ ($4049 \times 10^6 \text{ kg}$) for the SAR, aliased buoy, and high-frequency buoy time series, respectively. The high-frequency buoy results have nearly twice the ice (salt) production as the SAR and aliased buoy results, while the aliased buoy results track very closely with the SAR results (less than 4% relative difference).

6. Discussion

[51] ISW is, to date, the only winter field experiment in the western Weddell Sea, so our findings are a noteworthy contribution to understanding mesoscale processes of this region and in planning future expeditions. While it is clear that no individual instrument can resolve all features of a process, it is of benefit to identify the extent of these limitations and their impact on the evaluation of key processes. Therefore we proceed below by examining the relationship between spatiotemporal scales of the geophysical processes observed and the spatiotemporal resolution of the instruments that measure these processes.

[52] We divide the discussion into two parts. First, we compare our results with those in the literature to get a larger perspective. Then, we look at an example of a small-scale event to identify specific issues contributing to the differences found from buoy- and SAR-derived new ice production rates.

6.1. Surface Fluxes From Other Studies

[53] The closest validation for our toy model is experiment 1 in the young sea ice formation study by *Melnikov* [1995] made at the ISW camp from 20 to 28 May (days 141 to 149). For ease of comparison, Table 3 lists the relevant

properties. The primary differences are the time period (March versus May) and air temperature (colder for *Melnikov* [1995]). Despite these differences, we find good agreement for water salinity and temperature.

[54] At first glance, the assumption $s_i = 0.31 s_w$ results in lower ice salinity than observed. This suggests too much salt and therefore an overestimate of salt production. However, the observed brine salinity reported by *Melnikov* [1995], which is implicitly included in our salinity relation, indicates significant brine loss (up to 40%) within a few days of ice formation. Unfortunately, the percentage of brine volume is not explicitly provided at each time interval in *Melnikov's* [1995] study. While we cannot quantitatively draw a conclusion, the above approximation qualitatively validates our solution.

[55] The last two rows in Table 3 are the range and median of new ice growth. The temperature ranges differ between these two studies, so a direct comparison is not possible. Instead, the ice thicknesses and times recorded by *Melnikov* [1995, Table 1] are used to estimate new ice growth rates. These computed values (Table 3) are commensurate with Figure 8b, with median values that give us confidence in the model we used. We believe that high winds may compensate for the warmer temperatures in our study relative to *Melnikov's* [1995] study when it was colder but less windy. This may account for the similarity in ice production rates. As a final comment, we note *Melnikov's* [1995, p. 4673] observation of “a 12-hour period of oscillatory motion during the first day of ice growth” as well as “a 1.5- to 2-hour oscillation in the skeletal layer of 28-cm ice.” These observations reiterate the significance of subdaily forcing on these small-scale ice processes.

[56] Scaling upward (Table 4), the *Eisen and Kottmeier* [2000] (hereinafter referred to as EK2000) study described earlier found a maximum monthly ice production of 30 cm or, on average, 1 cm d^{−1} over the thin and open water sections over the entire western Weddell Sea based on their kinematic/thermodynamic model using 6 hourly European Centre for Mid-Range Weather Forecasting (ECMWF) fields and buoy motion over a 9 year period. The average new ice growth rate over the 12 day time series reported here is 4.3 cm d^{−1} using hourly observations and is therefore a factor of four greater than reported by EK2000. The monthly ice production by EK2000 is temporally smoother and includes a longer time period than either this or *Melnikov's* [1995] study and as such represents the longer timescales. An important sensitivity run by EK2000 was the filtering of tides using a 36 hour filter on the buoy divergence fields while still maintaining the 6 hourly ECMWF temporal resolution. In that scenario,

Table 4. Comparison With Other Studies

Study	Growth Rate, cm d^{-1}	Timescale	Space Scale
<i>Melnikov</i> [1995]	5.2	hourly	small scale
This study	5.4	hourly	mesoscale
<i>Eisen and Kottmeier</i> [2000]	1	four times daily	large scale
<i>Markus et al.</i> [1998]	0.4	daily	large scale

EK2000 shows a decrease in salt production by $\sim 25\%$ in the western Weddell Sea. This corroborates our findings of divergence and new ice production sensitivity to temporal resolution.

[57] Finally, we consider the 3 year Weddell Sea coastal polynyas study from 1992 to 1994 (M98). Using the same energy balance described in section 5 and SSM/I images at 25×25 km resolution, M98 found an ice extent for the Weddell Sea in early to mid-March 1992 of 2×10^6 km² (M98, Figure 13) and, using their 1 m average ice thickness assumption, a total ice volume of 2×10^{12} m³ (M98, Figure 14a). The total polynya area was about 2% of the ice extent (M98, Figure 14c), or 40,000 km², with their average monthly ice production in Weddell Sea polynyas during March 1992 of 5×10^9 m³ (M98, Figure 13). In terms of average daily new ice production rates, this value is $\sim 16 \times 10^7$ m³ d⁻¹ or 0.4 cm d⁻¹ within polynyas. This value is substantially less (roughly half) than the EK2000 study and an order of magnitude less than this and *Melnikov's* [1995] studies.

[58] We note two key issues contributing to the low M98 results. First, the M98 heat flux values are computed using the ECMWF analysis fields. As reported by M98 and by participants in ISW (S. Ackley, personal communication, 1993), wind velocity and direction from the three meteorological buoys from ISW were incorporated into the ECMWF analysis fields while the temperature records were withheld “by rejection or very low weights of temperature data in the assimilation scheme” (M98, p. 280) such that ECMWF fields are as much as 10 K warmer than the in situ records available for this study. We corroborate by noting from M98 (Figure 11a) that the average monthly heat flux for March 1992 is around 100 W m^{-2} , while the average heat flux over the 12 day period in Figure 8 is about 175 W m^{-2} .

[59] A second issue is the use of daily averaged heat fluxes in the M98 study, while this study used hourly readings and EK2000 used 6 hourly analysis fields. During storm events (e.g., Figure 6), temperatures in this study plummeted by 20 K in a matter of hours, then rose again, resulting in heat fluxes exceeding 400 W m^{-2} (e.g., days 63 to 64 in Figure 8b), in contrast to the ECMWF daily mean of 100 W m^{-2} . The impact of these differences in temperature fields is perhaps best illustrated in the model sensitivity runs from EK2000. Their results show that a uniform temperature increase of 1 K causes a change of 25% in heat flux and 45% in ice growth rates. We therefore conclude that estimates of new sea ice production are particularly sensitive to instrument sampling rates and smoothing techniques, which must be considered in combination with the natural variability of new ice production rates.

6.2. Significance of Small-Scale Open Water Events

[60] Figure 9a shows a region of sea ice at the beginning of the storm, including a small region of open water (~ 3 km across). Six days later (Figure 9b), there is a 15- to 20-km-long by 0.5-km-wide serpentine lead (as determined by its

backscatter characteristics). The initial open water feature has frozen over. Ice features to the right of the open water section show evidence of shear motion in the medium to large floes, suggesting that the open water was initially held open through mechanical forces working between ice floes. The changes in composition are due to thermodynamic and kinematic processes at time intervals too short to be resolved with ERS-1 SAR. The rate of change of such features can easily account for differences in the open water fraction and resultant ice production rates shown in Figure 8.

[61] This example illustrates the difficulty of resolving important small-scale processes in the western Weddell Sea. On one hand, SAR images provide periodic snapshots of a dynamic ice field, making it impossible to fully capture the time evolution of small-scale, high-frequency processes. On the other hand, the buoy array captures high temporal variability but is limited in spatial resolution. Efforts to synthesize both data types through models are needed to resolve these small-scale, high-frequency processes. A very simple synthesis is demonstrated in Figure 8a, where the buoy divergence time series is calibrated intermittently using high-spatial-resolution SAR to estimate the initial open water fraction, and then heat fluxes are resolved from the bulk formulas (Figure 8b) to estimate ice and salt production (Figure 8c). This is possible because the correlation length scales of sea ice drift and divergence are on the order of tens to hundreds of kilometers. Such adaptations therefore provide effective model parameterization tools.

[62] For this study, sea ice composition (i.e., ice types: pancakes, individual free-drifting ice floes, aggregate-scale floes, and large plate structures) is of smaller scale than the forcing scale and as a result optimally responds to storm and tidal forcing to produce the large observed surface fluxes. Similar evidence for this process is demonstrated by *Geiger et al.* [1998a, Figure 12], where sea ice shear and divergence in the tidal frequencies dampen out as the season progresses from austral autumn into winter. Through that period, the ice composition changes from small floes to aggregate-scale features with leads and cracks, to large-scale plates of ice. This connection has also been made by *McNutt and Overland* [2003]. Furthermore, *Kwok et al.* [2003] show a small seasonal damping of tidal/inertial oscillations in the Arctic, with the implication that semidiurnal oscillations may now be stronger as a consequence of general ice thinning in the Arctic. Hence the scale of sea ice composition and its thickness may be a necessary parameter for surface flux variability, together with ice tidal/inertial divergence/convergence cycling strength, especially in the development of next generation “lead-oriented” ice models and implications of process changes in climate change scenarios.

7. Concluding Remarks

[63] The present study addresses the four questions posed in the introduction. We found answers to question 1 through

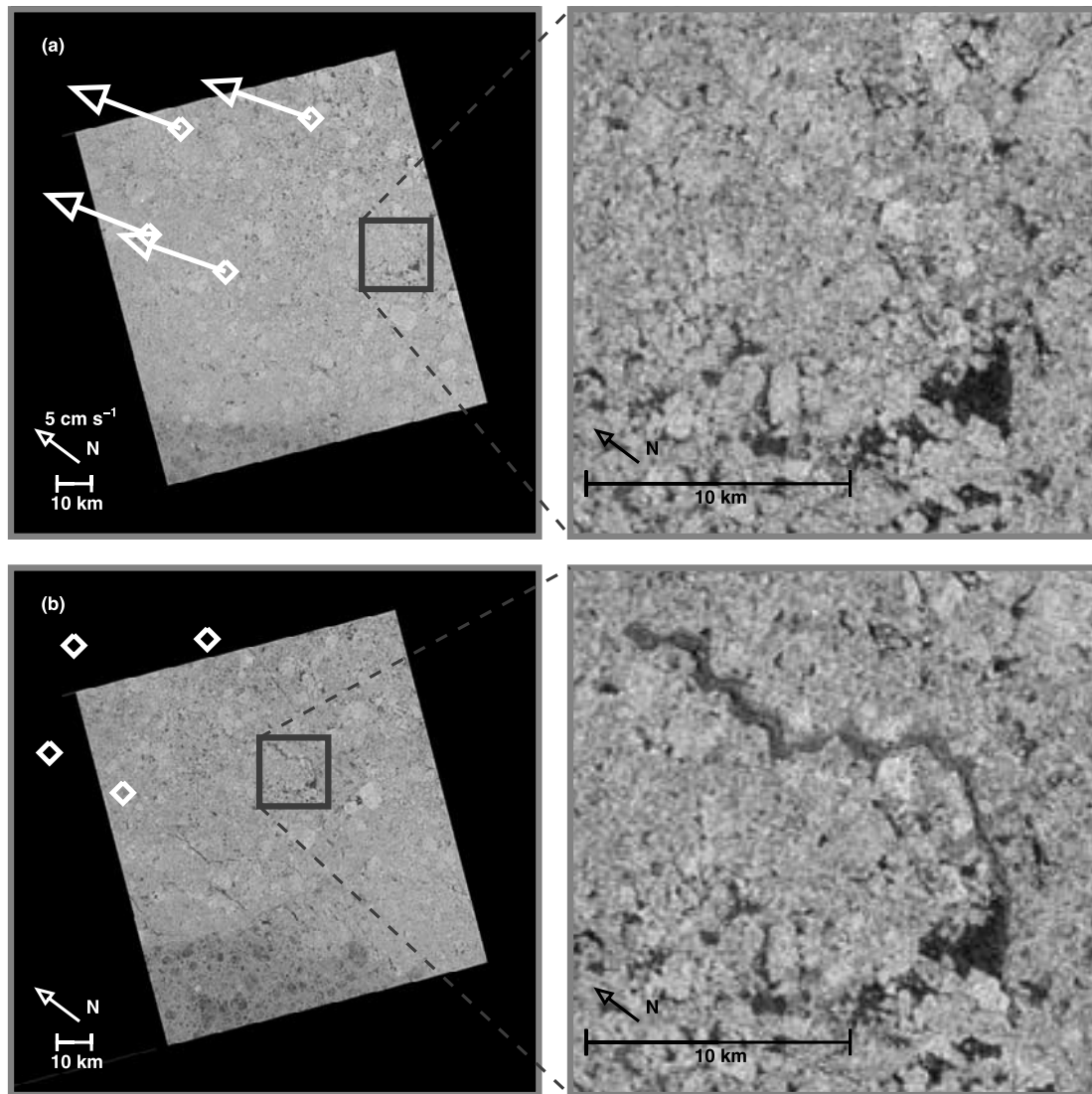


Figure 9. Example SAR images from day (a) 64 and (b) 70 projected on the SSM/I grid oriented relative to Greenwich. The position and orientation of both images are geographically nearly identical (see Table 1). White diamonds identify buoy positions, while arrows show buoy displacements as example motion between this image pair.

careful matching of temporal and spatial scales of SAR-derived motion products and buoys. We addressed question 2 through a difference study to isolate specific physical processes unresolved by SAR-derived products, in particular, those that affect surface flux estimates. Through that effort, we saw the nonlinear interaction of ice mechanics and high surface fluxes during winter storms along the western Weddell Sea continental slope. We responded to question 3 using a composite of information from buoys, SAR, and a bulk thermodynamic formulation to test the impact of ice divergence temporal resolution on ice production rates. From that experiment, we found nearly twice the new ice production rates when we used divergence incorporating subdaily variability.

[64] In the discussion, we responded to question 4 addressing three important issues. First, the consensus in the literature is that nearly half the surface flux in the Weddell Sea occurs in coastal polynyas, while equal

amounts can be accounted for in the small leads and cracks, especially those along the western shelf/slope. This leaves only a small amount, if any, of the flux through ice floes themselves, which cover 90% or more of the surface. There also remains a large discrepancy in new ice production rates (differing by as little as twice and by at least as much as one order of magnitude). Table 4 suggests that these discrepancies are widespread, with lower production rates at longer temporal scales. Dynamic processes on short timescales over a very large region are the obvious cause. Second, a small-scale open water event illustrates the nonlinear interaction of atmospheric, ice, and oceanic processes, specifically, regarding temporal and spatial scales and the impact of these small-scale processes on the general circulation. Third, aliased high-frequency motion introduces a bias in estimates of satellite-derived motion products, and this, in turn, affects remotely sensed surface flux estimates. With specific regard to ERS-1/2 data during the ice phase (3 day

exact repeat orbit), it is necessary to look at orbit crossovers to resolve any tidal component of ice drift (an important data component used in this case study).

[65] Parameterizations such as fetch and collection depth [Pease, 1987] have been developed but not integrated into the bulk formula models. As observed by Geiger *et al.* [1998b], subdaily processes are difficult to incorporate into many of the standard sea ice models without reconsideration of the boundary layer. Hibler *et al.* [1999] clarifies that the traditional slab method (i.e., wherein sea ice sits on top of the Ekman layer) dampens subdaily oscillations, making it impossible to resolve tidal features in a numerical simulation. To compensate for this, their Lagrangian experiment embeds sea ice into the Ekman layer, with inertial oscillations resulting [Heil and Hibler, 2002]. Incorporating similar methods into other sea ice models is a necessary condition prior to implementation of any lead parameterization. Finally, model implementation of these processes may require a variable-scale or embedded-scale grid (e.g., finite element or discrete element model) optimized to capture the appropriate temporal and spatial scales, particularly in areas of intensive subdaily activity.

[66] The next question, of course, is where to go from here? Reducing the temporal resolution of buoys and the spatial resolution of SAR to mutual levels compares well, as shown in section 3. However, a more effective combination is the synthesis of the two data sets to make use of the high spatial resolution of SAR and the high temporal resolution of buoys. While this remains an unsolved problem, the latter approach can be used to address tidal aliasing, either by crafting a joint buoy/satellite experiment over a time period of at least a few months or by using adjacent satellite tracks (as opposed to exact revisit orbits) to increase the temporal resolution of satellite-derived motion products. Adjacent tracks, especially from the larger swath width of RADARSAT (500 km), allow for a smaller time sampling interval (as little as 100 min) while still resolving a large number of motion vectors.

[67] A comprehensive tidal analysis requires a significant space agency (e.g., CSA, ESA, NASA) commitment in terms of acquisition of large volumes of wide-swath SAR data to properly resolve subdaily ice motion and the consequent ice growth deficit. A recent preliminary analysis by Kwok *et al.* [2003] shows that this is possible with RADARSAT wide-swath images within a direct line of sight to the ASF receiving station. However, the location of that study is particularly fortuitous in terms of the latitudinal location and the large number of overlapping orbits. The challenge, therefore, remains to conduct a similar experiment over a large geographic extent around the continental shelf of Antarctica, focused particularly on known dense water formation regions experiencing strong tidal and inertial forcing. In this context, the newly implemented wide-swath Global Mapping Mode of Envisat may become of significant interest because of its potential for obtaining daily coverage of significant portions of the Arctic and Antarctic sea ice cover.

[68] **Acknowledgments.** C.A.G. performed this work at the University of Delaware with support from NSF grant OPP9818645. M.R.D. performed this work at the Jet Propulsion Laboratory, California Institute of Technology, with support from NASA Polar Programs and at the European Space Agency (ESA)-ESTEC. ERS SAR data were kindly

provided by the German Processing and Archiving Facility as part of ESA studies A01.PIP.Ant3 and A02.U.S.A.119, copyright ESA. Special thanks to Laurie Padman and Robin Robertson for engaging discussions on tides in the Weddell Sea and other useful comments to the draft manuscript. Further thanks to the anonymous reviewers, whose comments led to improvements, the AGU Editors (Peter Schlosser and John Klinck), and especially the AGU Associate Editors (Hajo Eicken and Igor Belkin) for their scientific and publishing guidance.

References

- Carmack, E. C. (1977), Water characteristics of the Southern Ocean south of the Polar Front, in *A Voyage of Discovery, G. Deacon 70th Anniversary Vol.*, edited by M. Angel, pp. 15–41, Elsevier, New York.
- Drinkwater, M. R. (1998a), Active microwave remote sensing observations of Weddell sea ice, in *Antarctic Sea Ice: Physical Processes, Interactions and Variability*, *Antarct. Res. Ser.*, vol. 74, edited by M. O. Jeffries, pp. 187–212, AGU, Washington, D. C.
- Drinkwater, M. R. (1998b), Satellite microwave radar observations of Antarctic sea ice, in *Analysis of SAR Data of the Polar Oceans*, edited by C. Tsatsoulis and R. Kwok, chap. 8, pp. 145–187, Springer, New York.
- Drinkwater, M. R., R. Kwok, D. Winebrenner, and E. Rignot (1991), Multi-frequency polarimetric synthetic aperture radar observations of sea ice, *J. Geophys. Res.*, *96*, 20,679–20,698.
- Eisen, O., and C. Kottmeier (2000), On the importance of leads in sea ice to the energy balance and ice formation in the Weddell Sea, *J. Geophys. Res.*, *105*, 14,045–14,060.
- Emery, W. J., and R. E. Thomson (1997), *Data Analysis Methods in Physical Oceanography*, Elsevier, New York.
- Foldvik, A., and T. Gammelsrød (1990), Notes on Southern Ocean hydrography, sea ice and bottom water formation, *Paleoecol. Paleoclimatol.*, *67*, 3–17.
- Foster, T. D., and E. C. Carmack (1976), Frontal zone mixing and Antarctic Bottom Water formation in the southern Weddell Sea, *Deep Sea Res.*, *23*, 301–317.
- Gammelsrød, T., A. Foldvik, O. A. Nost, O. Skagseth, L. G. Anderson, E. Fogelqvist, K. Olsson, T. Tanhua, E. P. Jones, and S. Osterhus (1994), Distribution of water masses on the continental shelf in the southern Weddell Sea, in *The Polar Oceans and Their Role in Shaping the Global Environment*, *Geophys. Monogr. Ser.*, vol. 85, edited by O. M. Johannessen, R. D. Muench, and J. E. Overland, pp. 159–176, AGU, Washington, D. C.
- Geiger, C. A., and M. R. Drinkwater (2001), Impact of temporal spatio resolution on sea ice drift and deformation, in *Scaling Laws in Ice Mechanics and Ice Dynamics, IUTAM Symposium*, edited by J. P. Dempsey and H. H. Shen, pp. 407–416, Springer, New York.
- Geiger, C. A., S. F. Ackley, and W. D. Hibler III (1997), Year-round pack ice in the Weddell Sea, Antarctica: Response and sensitivity to atmospheric and oceanic forcing, *Ann. Glaciol.*, *25*, 269–275.
- Geiger, C. A., S. F. Ackley, and W. D. Hibler III (1998a), Sea ice drift and deformation processes in the western Weddell Sea, in *Antarctic Sea Ice: Physical Processes, Interactions and Variability*, *Antarct. Res. Ser.*, vol. 74, edited by M. O. Jeffries, pp. 141–160, AGU, Washington, D. C.
- Geiger, C. A., W. D. Hibler III, and S. F. Ackley (1998b), Large-scale sea ice drift and deformation: Comparison between models and observations in the western Weddell Sea during 1992, *J. Geophys. Res.*, *103*, 21,893–21,914.
- Geiger, C. A., Y. Zhao, A. K. Liu, and S. M. Häkkinen (2000), Large-scale comparison between buoy and SSM/I drift and deformation in the Eurasian Basin during winter 1992–1993, *J. Geophys. Res.*, *105*, 3357–3368.
- Gill, A. (1973), Circulation and bottom water production in the Weddell Sea, *Deep Sea Res.*, *20*, 111–140.
- Gloersen, P. (1995), Modulation of hemispheric sea ice cover by ENSO events, *Nature*, *373*, 503–506.
- Gordon, A. L. (1998), Western Weddell Sea thermohaline stratification, in *Ocean, Ice, and Atmosphere: Interactions at the Antarctic Continental Margin*, *Antarct. Res. Ser.*, vol. 75, edited by S. Jacobs and R. Weiss, pp. 215–240, AGU, Washington, D. C.
- Gordon, A. L., B. Huber, H. Hellmer, and A. Field (1993), Deep and bottom water of the Weddell Sea's western rim, *Science*, *262*, 95–97.
- Heil, P., and W. D. Hibler III (2002), Modeling the high-frequency component of Arctic sea ice drift and deformation, *J. Phys. Oceanogr.*, *32*, 3039–3057.
- Hibler, W. D., III (1979), A dynamic thermodynamic sea ice model, *J. Phys. Oceanogr.*, *9*, 815–846.
- Hibler, W. D., III, and K. Bryan (1987), A diagnostic ice-ocean model, *J. Phys. Oceanogr.*, *17*, 987–1015.
- Hibler, W. D., III, and E. M. Schulson (2000), On modeling the anisotropic failure and flow of flawed sea ice, *J. Geophys. Res.*, *105*, 17,105–17,120.

- Hibler, W. D., III, P. Heil, and V. I. Lytle (1999), On simulating high-frequency variability in Antarctic sea ice dynamic models, *Ann. Glaciol.*, *27*, 443–448.
- Hines, W. W., and D. C. Montgomery (1990), Multiple regression, in *Probability and Statistics in Engineering and Management Science*, 3rd ed., chap. 15, pp. 487–558, John Wiley, Hoboken, N. J.
- Holt, B., D. A. Rothrock, and R. Kwok (1992), Determination of sea ice motion from satellite images, in *Microwave Remote Sensing of Sea Ice*, *Geophys. Monogr. Ser.*, vol. 68, edited by F. Carsey, pp. 343–354, AGU, Washington, D. C.
- Jones, H., and J. Marshall (1993), Convection with rotation in a neutral ocean: A study of open-ocean deep convection, *J. Phys. Oceanogr.*, *23*, 1009–1039.
- Kottmeier, C., and L. Sellmann (1996), Atmospheric and oceanic forcing of Weddell Sea ice motion, *J. Geophys. Res.*, *101*, 20,809–20,824.
- Kowalik, Z., and A. Y. Proshutinsky (1994), The Arctic Ocean tides, in *The Polar Oceans and Their Role in Shaping the Global Environment*, *Geophys. Monogr. Ser.*, vol. 85, edited by O. M. Johannessen, R. D. Muench, and J. E. Overland, pp. 137–158, AGU, Washington, D. C.
- Kwok, R., and G. F. Cunningham (1994), Backscatter characteristics of the winter ice cover in the Beaufort Sea, *J. Geophys. Res.*, *99*, 7787–7802.
- Kwok, R., E. Rignot, B. Holt, and R. G. Onstott (1992), Identification of sea ice types in spaceborne synthetic aperture radar data, *J. Geophys. Res.*, *97*, 2391–2402.
- Kwok, R., S. V. Nghiem, S. H. Yueh, and D. D. Huynh (1995), Retrieval of thin ice thickness from multifrequency polarimetric SAR data, *Remote Sens. Environ.*, *51*, 361–374.
- Kwok, R., G. F. Cunningham, and W. D. Hibler III (2003), Sub-daily sea ice motion and deformation from RADARSAT observations, *Geophys. Res. Lett.*, *30*(23), 2218, doi:10.1029/2003GL018723.
- Levine, M. D., L. Padman, R. D. Muench, and J. H. Morison (1997), Internal waves and tides in the western Weddell Sea: Observations from Ice Station Weddell, *J. Geophys. Res.*, *102*, 1073–1089.
- Lindsay, R. W., and H. L. Stern (2003), The RADARSAT Geophysical Processor System: Quality of sea ice deformation estimates, *J. Atmos. Oceanic Technol.*, *20*, 1333–1347.
- Lytle, V. I., and S. F. Ackley (1996), Heat flux through sea ice in the western Weddell Sea: Convective and conductive transfer processes, *J. Geophys. Res.*, *101*, 8853–8868.
- Markus, T., C. Kottmeier, and E. Fahrbach (1998), Ice formation in coastal polynyas in the Weddell Sea and their impact on oceanic salinity, in *Antarctic Sea Ice: Physical Processes, Interactions and Variability*, *Antarct. Res. Ser.*, vol. 74, edited by M. O. Jeffries, pp. 273–292, AGU, Washington, D. C.
- Marshall, J., C. Hill, L. Perelman, and A. Adcroft (1997), Hydrostatic, quasi-hydrostatic, and nonhydrostatic ocean modeling, *J. Geophys. Res.*, *102*, 5733–5752.
- Martin, S., and P. Kaufmann (1981), A field and laboratory study of wave damping by grease ice, *J. Glaciol.*, *27*, 283–314.
- Maykut, G. (1986), The surface heat and mass balance, *NATO ASI Ser., Ser. B*, *146*, 489–549.
- McNutt, S. L., and J. E. Overland (2003), Spatial hierarchy in Arctic sea ice dynamics, *Tellus, Ser. A*, *55*, 181–191.
- Mellor, G. L., and S. Häkkinen (1994), A review of coupled ice-ocean modeling, in *The Polar Oceans and Their Role in Shaping the Global Environment*, *Geophys. Monogr. Ser.*, vol. 85, edited by O. M. Johannessen, R. D. Muench, and J. E. Overland, pp. 21–31, AGU, Washington, D. C.
- Melnikov, I. (1995), An in situ experimental study of young sea ice formation on an Antarctic lead, *J. Geophys. Res.*, *100*, 4673–4680.
- Padman, L., and C. Kottmeier (2000), High-frequency ice motion and divergence in the Weddell Sea, *J. Geophys. Res.*, *105*, 3379–3400.
- Padman, L., A. J. Plueddemann, R. D. Muench, and R. Pinkel (1992), Diurnal tides near the Yermak plateau, *J. Geophys. Res.*, *97*, 12,639–12,652.
- Parkinson, C., and W. Washington (1979), A large-scale numerical model of sea ice, *J. Geophys. Res.*, *84*, 311–336.
- Pease, C. H. (1987), The size of wind-driven coastal polynyas, *J. Geophys. Res.*, *92*, 7049–7059.
- Perovich, D. K., and B. Elder (2002), Estimates of ocean heat flux at SHEBA, *Geophys. Res. Lett.*, *29*(9), 1344, doi:10.1029/2001GL014171.
- Perovich, D. K., B. C. Elder, K. J. Claffey, S. Stammerjohn, R. Smith, S. F. Ackley, H. R. Krouse, and A. J. Gow (2004), Winter sea-ice properties in Marguerite Bay, Antarctica, *Deep Sea Res., Part II*, *51*, 2023–2039.
- Rignot, E., and M. R. Drinkwater (1994), Winter sea ice mapping from multi-parameter synthetic aperture radar, *J. Glaciol.*, *40*, 31–45.
- Rintoul, S. R., C. W. Hughes, and D. Olbers (2001), The Antarctic Circumpolar Current System, in *Ocean Circulation and Climate: Observing and Modelling the Global Ocean*, *Int. Geophys. Ser.*, vol. 77, edited by G. Siedler, J. Church, and J. Gould, pp. 271–302, Elsevier, New York.
- Robertson, R., L. Padman, and G. D. Egbert (1998), Tides in the Weddell Sea, in *Antarctic Sea Ice: Physical Processes, Interactions and Variability*, *Antarct. Res. Ser.*, vol. 74, edited by M. O. Jeffries, p. 341–369, AGU, Washington, D. C.
- Smith, A. J. E., B. A. C. Ambrosius, and K. F. Wakker (2000), Ocean tides from T/P, ERS-1, and GEOSAT altimetry, *J. Geod.*, *74*, 399–413.
- Thorndike, A. S. (1986), Kinematics of sea ice, *NATO ASI Ser., Ser. B*, *146*, 489–549.
- Timmermann, R., A. Beckmann, and H. H. Hellmer (2001), The role of sea ice in the fresh-water budget of the Weddell Sea, Antarctica, *Ann. Glaciol.*, *33*, 419–424.
- Whitworth, T., III, A. H. Orsi, S.-J. Kim, and W. D. Nowlin Jr. (1998), Water masses and mixing near the Antarctic slope front, in *Ocean, Ice, and Atmosphere: Interactions at the Antarctic Continental Margin*, *Antarct. Res. Ser.*, vol. 75, edited by S. Jacobs and R. Weiss, pp. 1–27, AGU, Washington, D. C.
- Willmott, C. J., S. G. Ackleson, R. E. Davis, J. J. Feddema, K. M. Klink, D. R. Legates, J. O'Donnell, and C. M. Rowe (1985), Statistics for the evaluation and comparison of models, *J. Geophys. Res.*, *90*, 8995–9005.

M. R. Drinkwater, Ocean/Ice Unit, European Space Agency, European Space Research and Technology Centre, Science and Applications Department, Earth Observation Programmes, Postbus 299, 2200 AG Noordwijk, Netherlands. (mark.drinkwater@esa.int)

C. A. Geiger, Snow and Ice Branch, Cold Regions Research and Engineering Laboratory, Environment Research and Development Center, 72 Lyme Road, Hanover, NH 03755, USA. (cathleen.a.geiger@erdc.usace.army.mil)

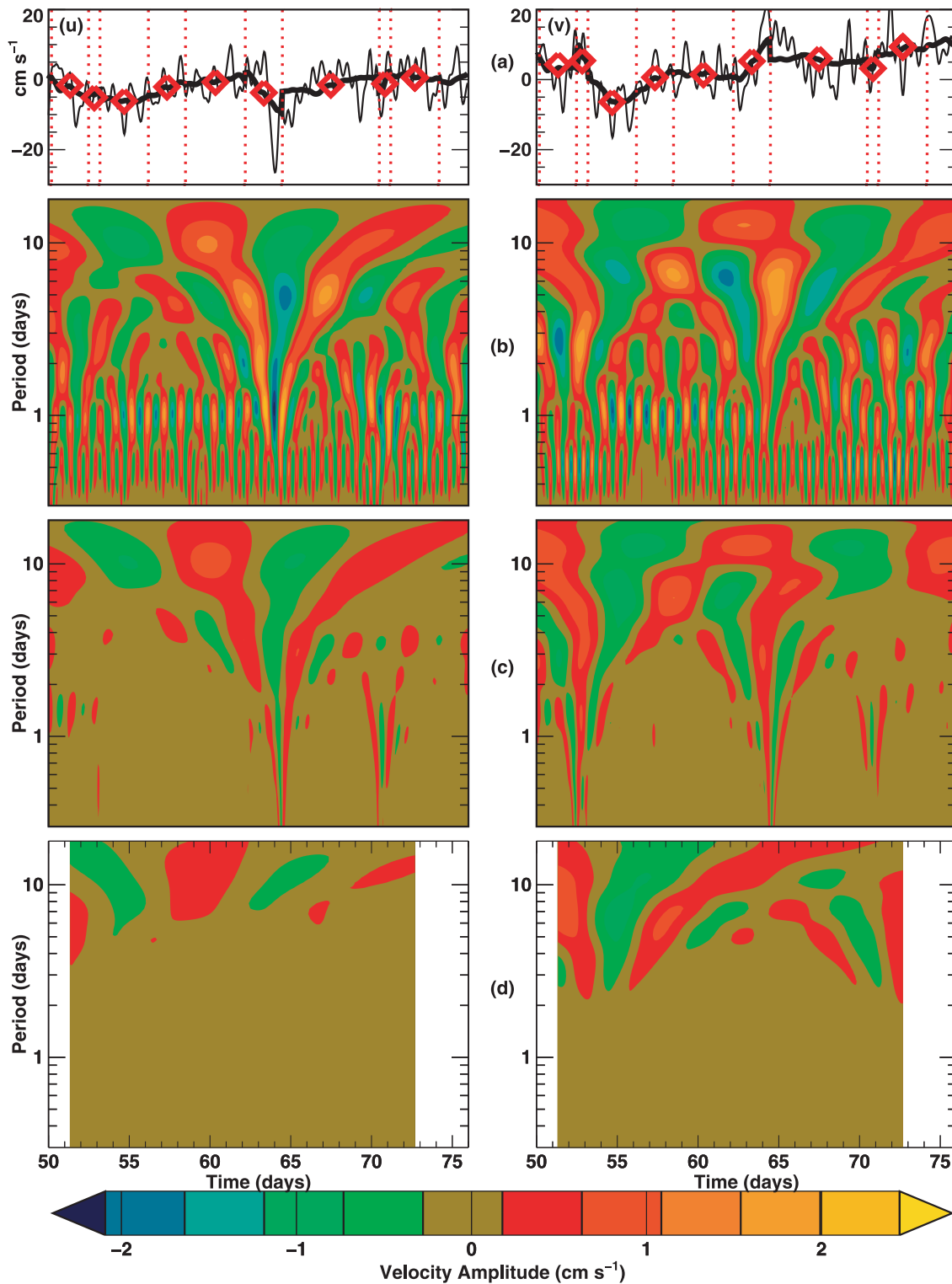


Figure 7. (a) Time series and (b–d) wavelet analysis of velocity components ((left) u and (right) v) from hourly buoy time series at the camp (thin line), aliased buoy time series (bold line), and the closest SAR motion vector (diamonds), with dotted vertical lines at SAR acquisition times. Spectrogram contours using the Morlet wavelet transform are plotted for the hourly buoy time series (Figure 7b), the aliased buoy times series (Figure 7c), and the closest SAR vector time series linearly interpolated (Figure 7d).